JOURNAL OF THERMOPHYSICS AND HEAT TRANSFER
Vol. 18, No. 1, January–March 2004

Measurement and Use of Reflectance Function Based on the Discrete-Ordinates Method

Mauricio A. Sanchez* and William H. Sutton†
University of Oklahoma, Norman, Oklahoma 73019

An experimental scatterometer based on the angular discretization of the discrete-ordinates or S_N method was constructed to account for the directional property of reflectance of metallic foils and their interaction with a high-temperature insulating material. Solution of the radiative heat-transfer equation is given in terms of the S_4 approximation taking into consideration a linear-anisotropic scattering function for the scattering characteristics of the fiber and including the directional properties of the foils as part of the boundary condition limits. Special treatment in the S_N method is required when dealing with directionally incident radiation in order to simulate the experimental conditions. The reflectance distribution function for the metallic surfaces showed to have a strong specular reflection and a weak diffuse component for all 12 incident directions in the spectral/gray model. Prediction of the reflectance function in fiber insulation while using measured reflectance data of the type of foil backing utilized provided good qualitative agreement. This is in lieu of the approximation in the scattering function and the directional biasing of the quadrature. However, using the full directional reflectance data helps to diminish this directional biasing (even intensity hemispherical distribution), which, in turn, leads to more consistent prediction of properties or to more accurate radiative-transfer calculations.

Nomenclature

A_m, B_m, C_m, D_m	=	intensity of radiation of mth octant in the y positive direction, A for positive x, z. B–D counterclock wise about positive y (Fig. 12)
A_x, B_y, C_z	=	control volume areas
AL, BL, CL	=	length in x, y, and z coordinates
$a_{\lambda 1}$	=	scattering slope factor of phase function
b_λ	=	backscattered parameter
$BRDF$	=	biangular reflectance distribution function
$C_{e\lambda}$	=	extinction cross section
$C_{s\lambda}$	=	scattering cross section
E_m, F_m, G_m, H_m	=	intensity of radiation of mth octant in the y negative direction, E for positive x, z. F–H counterclock wise about negative y (Fig. 12)
$E(x, y)$	=	fiber orientation
f	=	spatial frequency
f_v	=	fractional fiber volume
I_b	=	planck function for emission
I^m	=	intensity of radiation regardless of octant
k_0	=	free space propagation constant
L	=	observation length of the surface or characteristic length
lc	=	autocorrelation length
m	=	effective complex refractive index
n	=	real part, complex refractive index
$N[r(x, y)]$	=	number of radii between r and $r + \mathrm{d}r$
$P(\Omega \rightarrow \Omega')$	=	phase function for scattering
q	=	heat flux
r	=	fiber radius or boundary direction
S^m	=	source function
s_i	=	directions of quadrature
V	=	control volume
X_0	=	sample thickness
x, y, z	=	Cartesian coordinates
x_i	=	fraction of fibers with radii between r and $r + \mathrm{d}r$
β_λ	=	volumetric extinction coefficient
ε	=	emissivity
η	=	component concentration
Θ	=	polar angle
κ	=	complex part, refractive index
$\kappa_{g\lambda}$	=	volumetric absorption coefficient
Λ	=	optical property through Brugeman's theory
λ	=	wavelength
ξ_m, η_m, μ_m	=	director cosines in m quadrature
ρ	=	reflectance
$\sigma_{s\lambda}$	=	volumetric scattering coefficient
τ	=	optical thickness
Φ	=	azimuthal angle
ψ	=	differencing parameter
Ω	=	directional angle–solid angle
ϖ_i	=	quadrature weights

Subscripts

b	=	backward face
e	=	east face
f	=	forward face
i	=	incident
m	=	quadrature direction
n	=	north face
o	=	optical
p	=	middle point
s	=	south faces or scattered by context
w	=	west face
λ	=	wavelength dependant

Superscripts

d	=	diffuse
s	=	specular
$+$	=	positive direction
$-$	=	negative direction
$'$	=	incoming or incident

Received 7 March 2003; revision received 1 July 2003; accepted for publication 5 July 2003.

*Professor, School of Aerospace and Mechanical Engineering, 865 Asp Avenue, Room 121. Member AIAA.

†Professor; currently Professor and Department Head, Mechanical Engineering, University of Alabama, 209 Hardaway Hall, Tuscaloosa, 35401. Member AIAA.

I. Introduction

FIRE barriers are often manufactured by layering alternating blankets of ceramic fiber insulation with bounding thin metallic foil sheets, which are utilized in the expansion gaps or joints in walls or floors. Typically almost 60% of the heat transfer in a fire is by radiation in thermal barriers and insulation materials; the rest is caused by conduction and convection. The accuracy of any prediction in combined modes of heat transfer is strongly dependent on the knowledge of the radiative properties of the materials involved in the energy exchange.[1] Despite the fact that considerable effort has been made in previous years to improve the theory behind thermal radiative property predictions, results are generally not valid for an entire range of surface and boundary conditions. In the case of surface conditions, complications arise in the surface roughness because of contamination. In the case of boundary conditions, there are little data available that take into account the interaction between surface properties with their surroundings. These reasons make the only reliable method of assessing thermal radiation properties through experiment.

The most important radiative property, which describes the reflection of radiation from a surface, is known as the bidirectional reflectance distribution function (BRDF), or simply reflection function. For the case of fiber insulations, volumetric properties and the scattering probability model are required to account for radiative-transfer predictions. For an analytical model one must account for the orientation of the fibers, the type of material (complex refractive index), the volumetric fraction related to thickness, and the independent/dependent scattering behavior of the individual fibers composing the insulation.

Reflection Function Determination

The metallic material of a fire barrier is the radiative boundary condition of the participating radiation problem. Many surfaces encountered in engineering practice possess a vast quantity of irregularities so that application of fundamental theories is neither practical to use nor accurate to obtain a complete representation of the reflectance function. Numerous studies and experiments have been developed in the area of optical or light scattering in rough surfaces.[2–10] Beckmann and Spizzinno[6] gave a complete approach in which they made use of the Kirchhoff-based relationship to derive the function for isotropic surfaces with a normal Gaussian-height distribution. Works by Torrance et al.[7] and Smith et al.[8] demonstrated the use of the work done by Bennet and Porteus[5] by conducting a series of experiments (using gonioreflectometers) and numerical analysis (using electromagnetic theory correlations) for which the reflectance function was determined. Their numerical results agreed well with the experimental values for the different surface reflectors. They showed that when the surface is rougher than permitted by the smooth-surface requirement (rough surfaces), meaning that the surface features are larger than the radiation wavelength, other approaches can be taken for the reflectance function determination.

Geometric optics is a numerical method that has been used with success to determine reflectance in very rough surfaces.[3,7–10] However, for surfaces that are less than very rough, with concentrated anisotropy in the profile, a common method to predict reflectance is by conducting light-scattering experiments. Experimentation can capture the reflectance function of any surface; the data extracted from it can be used, not only for surface profilometry but also for surface defect detection.[11]

Analysis of Fibrous Materials

The detailed study of radiative heat transfer in fibrous materials began around 1955. Despite the fact that much research was concerned with only conduction through the gas and solid phases of high-porosity materials, it was noted that radiation plays an important role in the determination of heat-transfer rate even at moderate temperatures.

Some early studies[12] treated experiments and theory for single scatter and applied the results to the radiation heat transfer. Tong[13] and Tong and Tien[14] developed a good approximation for the effects on radiation and conduction heat transfer in fibrous materials.

Lee[15–17] and Lee and Cunnington,[18] considering the two-dimensional characteristics of a fiber and the orientation of the fiber, developed the phase function for scattering and the integration of the radiative properties using Maxwell's equations for electromagnetic scattering in infinite cylinders for any particular orientation. For single scatter the phase function for scattering exhibits a strong peak in the direction of incident radiation,[16] which is an indication of highly anisotropic material. A new model for independent and dependent radiation heat transfer in fibrous material that is more accurate than for previous investigators was also developed.[18]

Numerical Scheme

The discrete ordinate method (DOM) has become one of the most popular current methods to solve radiative heat-transfer problems involving scattering. Because of its ease of application, it can be incorporated with commercial computational-fluid-dynamics codes, and it requires similar formulation if accuracy needs to be increased.

Early application of DOM noted a redistribution of radiative energy in angular directions unless careful attention was given to the representation of angular integration. Directed beams in multidimensional geometries (such as with lasers) and Fresnel-type reflective boundaries can produce such ray effects. Enhancements of the DOM have been applied to overcome these difficulties.

Several numerical schemes in which a biangular reflectivity or Fresnel-type boundary is applied have been developed for one-dimensional Cartesian geometries[19,20] and cylindrical coordinates.[21] Roux and Smith[19] made use of the discrete ordinates method to obtain biangular reflectance on a one-dimensional substrate. Using Ambarzumian's method, Rokhasaz and Dougherty[20] obtained a solution for radiative transfer within a homogeneous, one-dimensional absorbing, isotropically scattering media with reflecting interfaces. An enhancement of the DOM was also proposed for a radiative-transfer medium with Fresnel boundaries.[21]

Objective

Measurement of the reflectance function has usually been performed using goniometric optical scattering instruments[7,8] because this apparatus can readily perform in-plane and out-of-plane measurements. However, with the aim of demonstrating a practical application, a much simpler prototype based on a hemispherical-scattering instrument[22] has been designed based on the DOM. The same apparatus will measure the interaction in reflectance function between different metallic foil backings and different optical thicknesses and orientation of the fiber insulation. The reflectance data obtained from this device can be directly applied to a DOM code when solving the radiative-transfer equation (RTE). The concept here is to better match experiment and theory.

A version of the fully symmetric DOM in a three-dimensional participating medium is formulated using a control volume formulation solution methodology that avoids apparent singularities in the RTE. Although this type of formulation is only applied to rectangular coordinates here, it can be extended to any geometry.

The discrete ordinate method in radiation is coupled to the experimental data as a validation of the properties for fire barrier materials. By using the experimental data from the simple scatterometer, a more detailed heat-transfer analysis for a fire barrier or to any of its components can be performed in order to get a more exact prediction of the radiation heat-transfer phenomena. Stability and accuracy of the solution are discussed for the problems presented here. Advantages and shortcomings of the solution are also noted.

II. Theory

Layers of metallic foil are often considered alone as thermal radiative shielding by reflecting heat. The foil also serves to minimize the direct hot gas flow from the fireside to the layer(s). For the fire barrier thin layers of foil are placed on the outside on an insulating blanket, in this case Durablanket® S fiberfrax (FF). A highly reflective foil metal works best. Aluminum foil (0.406 mm thick) is a good candidate because it is highly reflective, but it cannot withstand the high fireside temperatures. Stainless-steel type 321 (0.102 mm thick) foil can also be used in conjunction with the aluminum because this material can be positioned at the outer layers of the multilayer fire

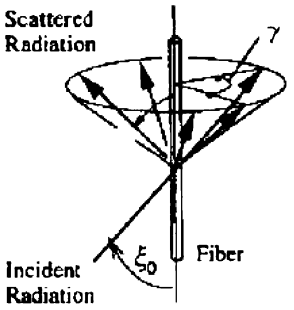

Fig. 1 Scattering by a single fiber.

barrier to withstand the direct temperatures involved in the fire. The characteristics of the foils are given in Ref. 23.

Thermal insulations are typically composed of fibers of some millimeters in length and several micrometers in diameter. The usual modeling of a fiber is an infinitely long cylinder (two-dimensional region) because the fiber length is much larger than both the diameter d and the wavelength λ of the radiation incident upon it. It is customary to obtain these parameters to define the absorption, scattering, and extinction parameters of the intensity in the participating media, because these properties will help to define the scattering. These models also take into consideration the orientation and size distribution of the fibrous material.

The spectral volumetric scattering coefficient $\sigma_{s\lambda}$ is defined as the fraction of incident radiation that is scattered by the particle in the hemisphere along the path of the beam. For a fiber the single scattering is given in terms of the scattering cross section $C_{s\lambda}$, as the effective area of scattering in a given direction.

The spectral volumetric absorption coefficient k_λ is defined as the fraction of incident radiation that is absorbed by the matter along the path of the beam. The extinction coefficient β_λ is defined as the sum of the absorption coefficient and the scattering coefficient. Solutions of the scattering of an infinitely long cylinder are well documented in the literature.[24] The extinction and scattering cross sections for unpolarized radiation at oblique incidence on an infinite cylinder as depicted in Fig. 1 are given by[18]

$$C_{e\lambda}(\xi_0) = \frac{2}{k_0} Re\left[\sum_{n=-\infty}^{\infty} (b_{n1} + a_{n2})\right] \tag{1}$$

$$C_{s\lambda}(\xi_0) = \frac{4}{k_0}\left[\frac{1}{2}\left(|b_{01}|^2 + |a_{02}|^2\right) + \sum_{n=1}^{\infty}\left(|b_{n1}|^2 + |a_{n2}|^2 + 2|a_{n1}|^2\right)\right] \tag{2}$$

where the coefficients a_n and b_n are function of the incident angle, size parameter, and the complex refractive index.

Depending upon the type of fiber insulation, these can be classified according to the fiber orientation. For instance, the fibers of commercial fiber insulation are randomly oriented in space, whereas some thermal blankets could have fibers oriented or aligned with respect to a plane. The specific orientation of the fiber relative to incident energy influences the radiative properties of the fiber, as demonstrated by Lee.[15]

For determination of the spectral extinction or scattering coefficient in a fiber media, the respective radiative cross sections must be weighted with respect to the size distribution and orientation, resulting in

$$(\beta_\lambda, \sigma_{s\lambda})(x, y) = \int_0^{2\pi}\int_0^{\pi/2}\int_{r_1}^{r_2} [C_{e\lambda}(\xi_0), C_{s\lambda}(\xi_0)]N \times [r(x, y)]F(x, y)\, \mathrm{d}r\, \mathrm{d}x\, \mathrm{d}y \tag{3}$$

$$\kappa_{a\lambda} = \beta_\lambda - \sigma_{s\lambda} \tag{4}$$

where x and y represent the directions of fiber orientation, $N[r(x, y)]$ is the number of fiber with radius between r and $r + \mathrm{d}r$, and $F(x, y)$ specifies the fiber orientation. This equation implicitly assumes that the fibers scatter independently.

For the solution of the RTE, the phase function for scattering must also be determined. For ease of application, the phase function for scattering is based on Tong[13] and Tong and Tien.[14] This model assumes that the scattering process of a fiber can be approximated by the scattering behavior of a sphere. Thus, the phase function for scattering is replaced by

$$P(\Omega \to \Omega) = 1 + a_{\lambda 1}\cos(\Omega) \tag{5}$$

Equation (5) states the radiation energy scattered from incident direction Ω' to the scattered direction Ω has a linear behavior with a factor of "slope" $a_{\lambda 1}$ as

$$a_{\lambda 1} = 2(1 - 2b_\lambda) \tag{6}$$

where the factor b_λ [Eq. (6)] is the backscattered parameter of the linearly anisotropic function, found by integrating Eq. (5) over the backward hemisphere.

$$b_\lambda = \int P(\Omega \to \Omega') \tag{7}$$

To solve Eqs. (3), (4), and (7) for the Durablanket S, some other physical properties must be utilized. This properties range from the spectral complex refractive index $\bar{m}$, to the fiber size distribution $N[r(x, y)]$, fiber orientation $F(x, y)$, and the volumetric fraction f_v.

The spectral complex index of refraction is $\bar{m} = n - ik$, where n is the real part, which accounts for the refraction of the radiation wave, and k is an imaginary part accounting for absorption, depends of the composition of the material. Durablanket S, with a specific gravity of 2.73 g/cm^3, is made of a chemical combination of silica and alumina. A simple approximation can describe the index of the small particles making up the material with an average of the indices of the two components, known as effective medium theory. An effective medium theory, through the use of the Brugeman's approximation,[25] treats the components of the medium in a symmetrical way. For a binary composition medium this approximation for a property can be stated as

$$\bar{m} = \tfrac{1}{4}\left(\Lambda + \sqrt{\Lambda^2 + 8\bar{m}_1\bar{m}_2}\right) \tag{8}$$

where $\Lambda = (3\bar{\eta}_1 - 1)\bar{m}_1 + (3\bar{\eta}_2 - 1)\bar{m}_2$ and $\bar{\eta}_1$ and $\bar{\eta}_2$ are the concentration of the components.

Using the indexes of refraction for silica and alumina,[26] a new index of refraction for Durablanket S with a composition of 55%, 45% silica, and alumina respectively is calculated and shown in Table 1. The results obtained from this theory establish that there exists a nonrandom effective value for the refractive index such that the properties of the system are the same as for a homogeneous system governed by the effective parameter values. The uncertainty

Table 1 Estimated complex refractive index of Durablanket S [55% S_iO_z, 45% Al_zO_3]

λ, μm	η	κ
0.500	1.598	0
0.633	1.594	0
1.0	1.583	0
2.0	1.568	0
3.0	1.640	0
4.0	1.513	0
5.0	1.464	0
6.0	1.396	0.001
7.0	1.254	0.002
8.0	0.780	0.257
9.0	1.137	1.175
10.0	1.741	0.214
11.0	1.024	0.257
12.0	0.929	0.759

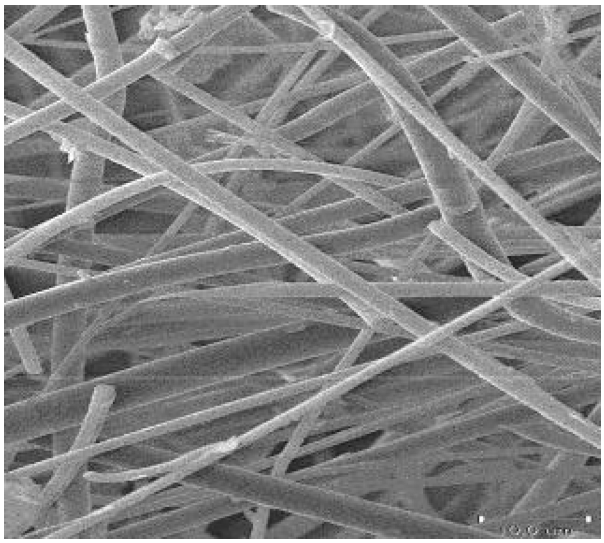

Fig. 2 SEM of Durablanket S fibers.

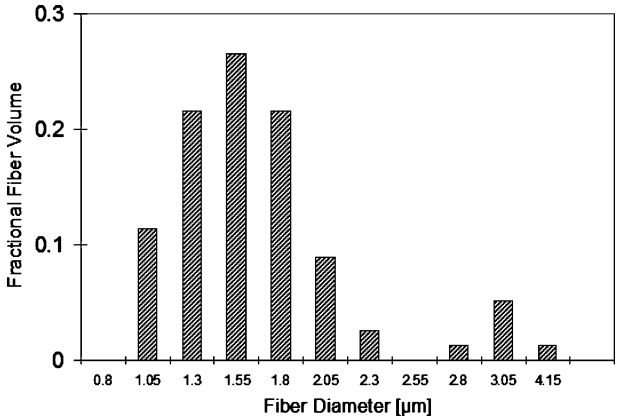

Fig. 3 Fiber size distribution Durablanket S.

of the Table 1 values is low because the approximation has none of the complicated details of the microstructure of the fiber.

The effective volumetric fraction f_v can be estimated by taking the ratio of the insulation density to solid the mass density. For Durablanket S, f_v yields a value of 4.27×10^{-2}.

Scanning electron microscopy (SEM) and microscopic counting determined both the fiber size distribution and the orientation of the fibers. Using an autoscan electron microscope and coating the fibers with carbon and silver-palladium, the fiber orientation $F(x, y)$ of the insulation are considered as fibers randomly oriented in space (Fig. 2). Fiber size distribution $N[r(x, y)]$ is shown in Fig. 3. Several SEM photographs were analyzed, and the number of individual fibers counted for the respective cases were greater than 80.

The size distribution gives an estimated mean diameter of 1.58 μm while the manufacturer's product data sheet states a fiber mean diameter of 2.5 to 3.5 μm. The manufacturer noted that the standard deviation of the fiber size distribution was very large between batches and that the published value is only a rough estimate of the actual fiber sizes. The surfaces of the individual fibers are relatively smooth, and the fiber length to diameter is consistent with the assumption of the property model as an infinite cylinder.

Knowing that the fibers are randomly oriented in space, there is no correlation between the size and orientation. Also, the radiative coefficients can be averaged over all angles of incidence for this reason. Equation (9) models the case of fibers randomly oriented in space[18] to calculate the radiative properties of infinite cylinders.

$$(\beta_{\lambda r}, \sigma_{s\lambda r}) = \frac{f_v}{\pi} \sum_{i=1}^{N} \frac{x_i}{r_i^2} \int_0^{\pi/2} [C_{e\lambda}(\xi_0), C_{s\lambda}(\xi_0)] \cos(\xi_0)\, \mathrm{d}\xi_0 \quad (9)$$

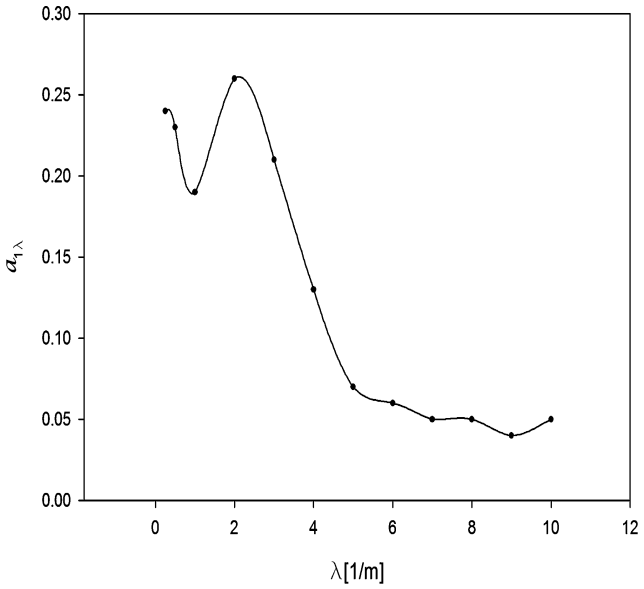

Fig. 4 Backscatter factor.

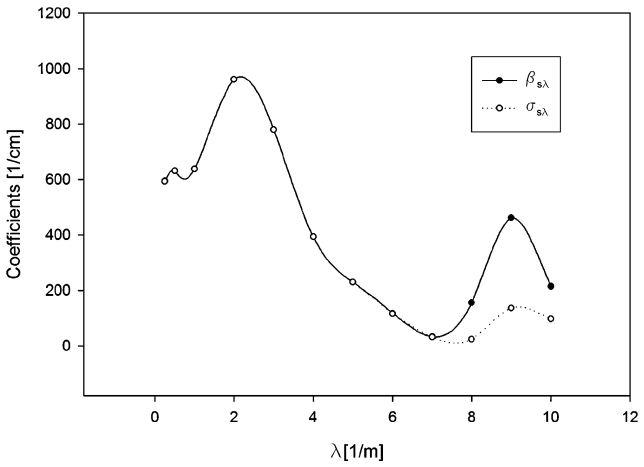

Fig. 5 Single scattering albedo Durablanket S.

Equations (3) and (4) were solved and compared using an algorithm created by Swathi and Tong[27] and cross correlated with the help of the Applied Sciences Laboratory, Inc., California (except backscatter factor, Fig. 4).

Figure 5 shows the spectral variation of the scattering and extinction efficiencies. The small values of the spectral scattering coefficient obtained through Eq. 9 at large wavelengths are produced by the closeness of the absorption coefficient in the refractive index range 8–10 μm. Furthermore, the values of the linear anisotropic parameter $a_{\lambda 1}$, represented through the backscatter factor, show that the anisotropic part of the scattering phase function is small, which leads to the conclusion that most of the scattering would be isotropic. Finally, the average gray values coefficients over the preceding wavelength range were determined and compared to the values used by Caplinger et al.[28]: [0.74–0.93] for the single scattering albedo and 4864 (1/m) for the extinction coefficient. The average backscatter factor is 0.470.

III. Instrument Description

Although the selection or choice of the quadrature scheme is arbitrary, a good quadrature should be one that not only integrates the RTE well, but also satisfies the zeroth, first, and second moments of a scattering phase functions of high complexity accurately. The S_4 quadrature approximation has been shown to work well for multidimensional heat-transfer problems with isotropic or simple scattering

phase functions including some of higher complexity.[29] The choice of the quadrature scheme for this experiment is the completely symmetric quadrature originally developed by Larthrop and Carlson.[30] Table 2 describes the S_4 quadrature used in this work.

Converting the numerical quadrature in Table 2 into degree angles produces a series of angles located at the bottom of the hemisphere (45, 71.96, and 18.04 deg), which represent the azimuthal angles Φ and the upper angles (24.74, 72.79, and 72.79 deg), representing the polar angles Θ measured from the z axis.

Figure 6a shows a top view of the collection shell of the DOM-hemispherical scatterometer. This hemispherical shell was made of spun aluminum and had an outside radius of 62 mm and a thickness of 1.3 mm. The roughened shell was flat black-anodized to obtain a near-blackbody configuration. Each quadrant of the hemispherical shell had three opening ports to locate either the sensor or the light source while using a zero-surface-depth coupling mechanism. Thus, although 11 ports held detection system, one port was being used as an incident source. The shell was attached to a black-anodized base where the samples would be placed. Each of the 12 sensors was laser aligned to point at the center of the sampling holding base.

In Fig. 6b the coordinate system is depicted for the incident and scattering directions. The polar incident and scattering angles Θ_i and Θ_s are measured from the normal surface angle (axis z), whereas the azimuthal incident and scattering angles Φ_i and Φ_s are defined with respect to the plane of incidence. Table 3 shows the actual location of the ports throughout the hemisphere.

Figure 6b also depicts the center support surface (base of the hemisphere) in which the specimen material will be aligned and placed. This surface region (see Fig. 7) is an adjustable section that will allow alignment, measurement, and assessment of light reflected from the metallic sample alone (Fig. 7a) and light transmitted and reflected from the a second sample, which is placed beneath a primary sample at the top of the surface in the center region (Fig. 7b).

The detection system consisted of a thin-film-based thermopile detector (Dexter Research®) model 2M with KBr window with

Table 2 Discrete ordinates completely symmetric quadrature[29]

Order of approximation	Ordinates		Weights	
	ξ	η	μ	ϖ
S_4	0.2958759	0.2958759	0.9082483	0.5235988
——	0.2958759	0.9082483	0.2958759	0.5235988
——	0.9082483	0.2958759	0.9082483	0.5235988

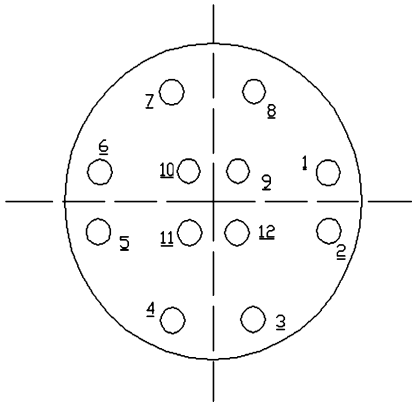

Fig. 6a Top view of the hemispherical detection holder showing multiple detection port positions.

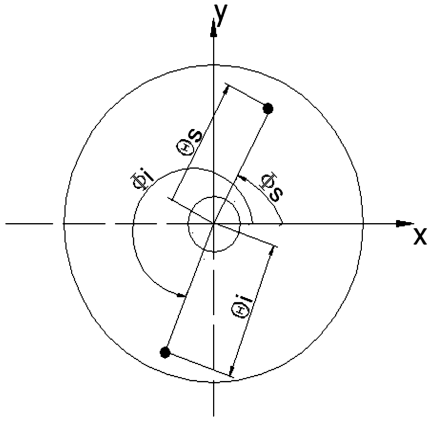

Fig. 6b Coordinate system projected into the holding surface used to describe the incident $\hat{i}$ and scattering $\hat{s}$ angles position.

Table 3 Direction of the detector center point

Port	Θ, deg	Φ, deg
1	73	18
2	73	342
3	73	288
4	73	252
5	73	198
6	73	162
7	73	108
8	73	72
9	25	45
10	25	135
11	25	225
12	25	315

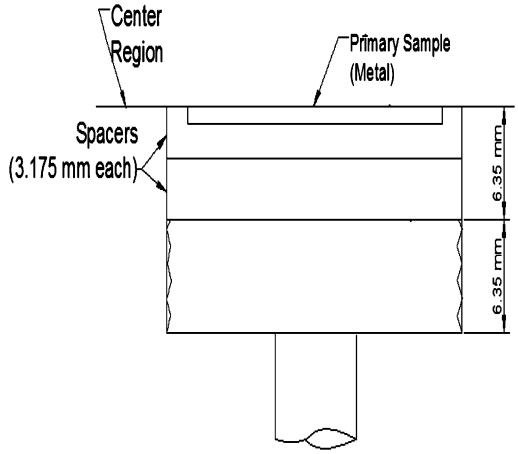

a)

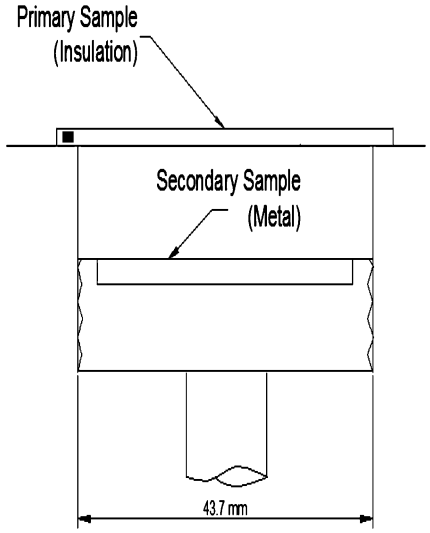

b)

Fig. 7 Sample-holder sections.

argon encapsulating gas. The voltage signal taken from the detectors was amplified through a low noise amplifier and acquired and recorded by a National Instrument® Data Acquisition System.

Three Ion Optics® infrared sources provided the incident power for the measurements. Each source could be varied over wavelength by changing the emitted power. Two of these sources are windowless (ReflectIR-P1N and TO-5) broad infrared light emitters that provide power for a wavelength range from 2 to 20 μm. These sources have a constant spectral distribution of 100% (based on a window transmission) for the entire wavelength range. The third light source is a collimated light source with a range in wavelength from 2 to 5.25 μm (ReflectIR-P1S) with an output pattern similar to the other collimated source ReflectIR-P1N. Although this source has a spectral distribution for the mentioned wavelength range greater than 80% based on window transmission, it mostly emits at 3 μm. An electronic device board and accompanied software are used to adjust the, temperature, amplitude, and frequency range of these infrared sources.

All light sources were set up at the same amplitude and frequency in order to increase the life expectancy of the source. However, the uncollimated (TO-5) and third light source (ReflectIR-P1S) were powered to work at a temperature of 600°C, whereas the second light source had a working temperature of 400°C. This temperature range was selected in order to obtain two working wavelength bands, taking into account the concepts of blackbody radiation functions and Wien's law.

The data-acquisition setup consists of the National Instrument system plus a multiplexing system, which allows scanning of 12 digital inputs using an eight-bit digital board and a Digital Tektronix® Oscilloscope. By using the same mechanism, temperature monitoring in the system was required in order to maintain isothermal operation.

System Calibrations and Experimental Procedure

According to the American Society for Testing and Materials designation E-1392-90,[31] the reflectance function can be measured and normalized using four types of normalizations schemes. It is the choice of this work to normalize the scattered power to the incident power in a relative manner. This relative technique normalizes the sample data to that of a reference standard or highly reflectance diffuse surface[31] with a known spectral reflectance function.

Because of the quality and characteristics of the detection system, the reflectance function can be obtained through the voltage signal ratio between the scattered and incident light intensity. Thus, there is no necessity to calibrate the sensors in an absolute basis. The normalization method for the scatterometer is accomplished by normalizing the instrument voltage response with the reference standard bidirectional reflectivity. This is calculated as[32]

$$\frac{\rho_{\lambda,\mathrm{spl}}(\Theta_i, \Phi_i; \Theta_s, \Phi_s)}{[\rho_{\lambda,\mathrm{ref}}(\Theta_i, \Phi_i; \Theta_s, \Phi_s)]} = \frac{V_{\mathrm{spl}}}{V_{\mathrm{ref}}} \tag{10}$$

where $\rho_{\lambda,\mathrm{spl}}(\Theta_i, \Phi_i; \Theta_s, \Phi_s)$ and V_{ref} represent the values measured by the scatterometer for the material sample to be investigated.

The experimental procedure was that voltage measurements were first taken in a black-anodized standard coupling with a length equal to the radius of the shell. By placing the light source at one side and the thermopile sensor at the other side, the registered voltage obtained from the sensor gives the total incident radiation (or reference voltage). The ratio between the thermopile detector area and the light source area was 1:1.35. Once the average incidence voltage was obtained, the light source was repositioned and aligned with respect to the DOM-hemispherical shell and measurements repeated. The background signals caused by the setup (hemisphere and fixturing) were subtracted from the baseline incident radiation.

Measurements were taken for all angles described in Table 3. After a series of repeated measurements yielded similar values, the data run was considered accepted. Each measurement takes a large number of samples, which are in turn are averaged.

Reference Standard

Because the working wavelength region is between the near infrared to the midinfrared, an Infragold® diffuse reflectance standard, from Labsphere, Inc., was selected to be the material reference for the relative measurements. The standard has a material coating with a high hemispherical reflectance value for this spectral region and provides sufficient energy levels over the entire range of incident angles.

The calibration from 2.5 to 15 μm every 50 nm is traceable to National Institute of Standards and Technology; the biangular reflectance for the Infragold was measured here with the same infrared sources used during the experiments.

Figure 8 shows the reflectance function for the reflectance standard for different types of sources. The calculated hemispherical reflectance, based on BRDF, was 97% compared to 99% stated by the manufacturer.

Uncertainty

Because the reflectance function was obtained through the ratio of voltage signals, there was great reduction in the overall uncertainty

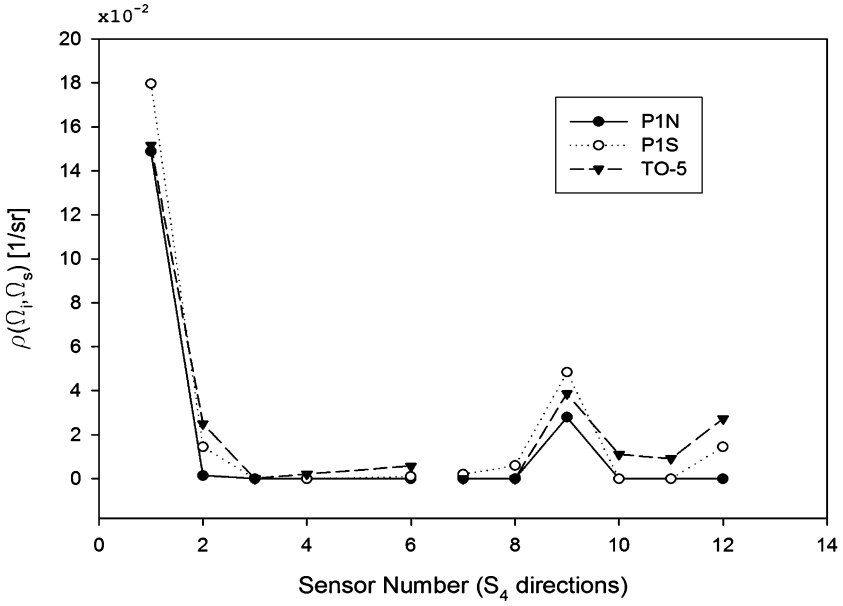

Fig. 8 Biangular reflectance function reflectance of Infragold using various light sources with incident angle of Θ = 73 deg and Φ = 18 deg (Port 1).

of the experiment. However, the contributions to this value can be summarized in the following paragraphs.

As just described, the sample materials to be analyzed were the aluminum foil, the 321-stainless steel, and the Durablanket S. Both metallic surfaces were carefully attached to the blackened holders (and thoroughly cleaned before sampling). Ensuring complete flatness of all samples was not possible. Reflectance values might be dependent of the flatness of the sample materials. However, samples were rotated 90 deg to characterize any orientation anomalies.

Erroneous readings can be generated if light enters at an unanticipated angle because the light might miss the center of the specimen. Great care was placed in the construction of the light source and all receiving area couplings to ensure that the light beam always enters directed toward to the specimen center. Because of the machining process of the hemispherical shell, the scattering or receiving angles (see Fig. 6) have an average deviation of $\pm\frac{1}{4}$ of a degree (± 0.005 radians) with respect to the exact values of the S_4 approximation. The contribution of this angular uncertainty and the solid-angle uncertainty can be considered small because each detector has the same solid angle (1.20×10^{-3} sr) and a large hole aperture that guarantees that the filed of view of the detector includes the entire sample irradiated area. However, this entire area might contain some small areas of the blackened surface where the samples are attached. This could contribute in the overall uncertainty of the reported reflectance values. The preceding factors, in addition to incident energy measurement, source and detector output variations (amplifier), and external setup components make the overall system bias of the uncertainty approximately 6.0%.

To eliminate noise signal from the detectors and contamination by other types of incident light, all measurements were taken at night in a cooled laboratory with blacked windows. To report accurate values of reflectance and to avoid noise equivalent reflectance [noise equivalent biangular reflectance distribution function (NEBRDF)], the measured voltage readings were compared against voltage readings when no sample holder section is placed at the bottom of the hemispherical shell. Depending on the type of source (especially uncollimated), some sensors detect incident light when no sample holder section was in place. These readings were subtracted from the actual sample readings in order to obtain the true reflectance for the respective sample.

To ensure more accurate and less noisy signals through the detectors, the signals were also recorded using Wavestart, a software package that connected the oscilloscope with the PC. These readings were compared with the Labview,™ readings and the less noisy signals were taken. By using a Gaussian filtering approach, the signals were denoised to obtain a smooth reading without losing the inherent details of the main signal. An average of 1400 data points per sample was collected through the oscilloscope for each detector to guarantee uniformity of the signals.

The use of the reference standard can also be a factor that increments the uncertainty of the data. Bias of the signals was calculated for each one of the obtained readings. Following the guidelines by Kim et al.,[33] the calculated statistical measurement uncertainty is around 4.2%. Using standard square root of the sum of the squares method for combining bias and statistical error, the combined uncertainty is approximately $\pm 7.39\%$.

Results and Discussion

Reflectance function measurements were performed on a series of sample materials that form a composite fire barrier. These measurements include all 12-port positions as incident angles. The samples were placed in the sample holder in the same direction in order to show if the anisotropy of the material possessed some effect in the reflectance.

To determine system effects between the insulation material and the metallic boundary or black boundary, reflectance measurements were performed, not only for every single one of the materials but also for each one of the possible combinations among the materials, that is, aluminum-insulation, black anodized surface-insulation, etc. Reflectance results for the metallic materials are reported in Ref. 23. The insulation material (FF) was rotated 90 deg to determine if there was any influence in the orientation position while keeping the bottom surface at the same orientation. All results were normalized using the specular value of the Infragold reflectance standard according to the incident port and light source used. However, in order to enhance the resolution of the results and reduce the uncertainty of the reflectance function of the Infragold, the data were renormalized using the average value of the hemispherical reflectance of the standard provided by the manufacture's calibration report.

Table 4 Durablanket S samples

Mass, g	X_0, cm	Designation, $f_v X_0$
1.4	0.424	0.0181
0.8	0.242	0.0103
0.4	0.121	0.0052

Despite the fact that the quadrature angles are similar for each quadrant, the experimental data have shown that there are preferential directions for scattering. For instance, angle positions labeled by ports 1, 5, and 7 always showed greater scattering values than the other ports. These could also be enhanced by some irregularities of the spinning of the shell. However, another possibility is that there exist preferential angles of scattering in the quadrature because for all light sources utilized in this work the same trend was observed for all sample materials. To better assess this claim, more in-depth experimentation might be carried out, perhaps using a bigger quadrature scheme or a precision goniometer.

Fiber Insulation

Reflectance data were taken for the Durablanket S fiberfrax (FF) insulation for three different optical thicknesses using the different light sources. This reflectance data were taken using different materials as a backing as just described in the experimental design of the sample holder section. Table 4 shows the different types of optical insulation thicknesses and their designation according to their mass. X_0 describes the measured and calculated thickness of each insulation sample. The preceding designation[18] [fiber volume fraction-thickness product ($f_v X_0$)] was chosen as adequate for analytical and numerical computations.

In spite of the 200°C of difference in the emission temperature from the Reflect IR-P1S collimated source with respect to the other two infrared sources, the behavior of the reflectance function trend of the fiber insulation was similar for the different surface backings and orientation for the upper angles of the quadrature. Figures 9 and 10 present the reflectance data among the combinations of fiber insulation and secondary surfaces. In these figures the backing makes an optically thin sample radiatively an optically thick one. The effect of fiber orientation with respect to the reflectance is small.

These experimental trials also show that for an optically thin sample ($f_v X_0 = 0.0052$) there were nonzero values of reflectance around the hemisphere (with respect to the 12 quadrature points). Because this particular sample has more transmittance than the others, the backing (secondary) surface seems to enhance the relative reflection function of the insulation.

IV. Mathematical Model

Considering the media as a rectangular form, the solution of the RTE is given in terms Cartesian coordinates for a rectangular enclosure containing a participating medium (Fig. 11). The RTE for this type of configuration cam be written as

$$(\Omega \cdot \nabla) I_\lambda(r, \Omega) = -(\kappa_\lambda + \sigma_{s\lambda}) I_\lambda(r, \Omega) + \kappa_\lambda I_b(r) + \frac{\sigma_{s\lambda}}{4\pi} \int_{\Omega' \to 4\pi} I_\lambda(r, \Omega) P(\Omega' \to \Omega)\, \mathrm{d}\Omega' \tag{11}$$

where $P(\Omega' \to \Omega)$ is the phase function of radiative energy transfer from the incident direction Ω' to the scattered Ω direction. The intensity of blackbody radiation for the medium at a given temperature is defined by the symbol $I_b(r)$; the spectral radiation heat-transfer coefficients are defined by the scattering coefficient $\sigma_{s\lambda}$ and

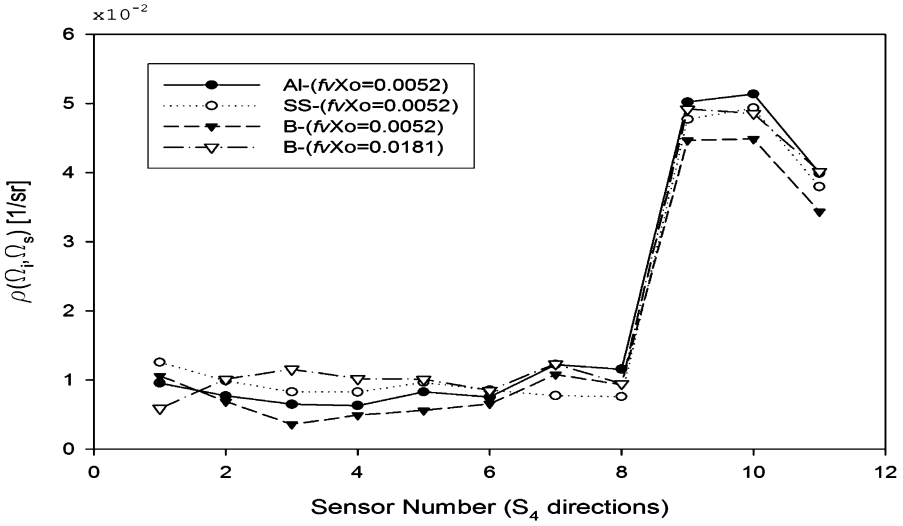

a) Position 1

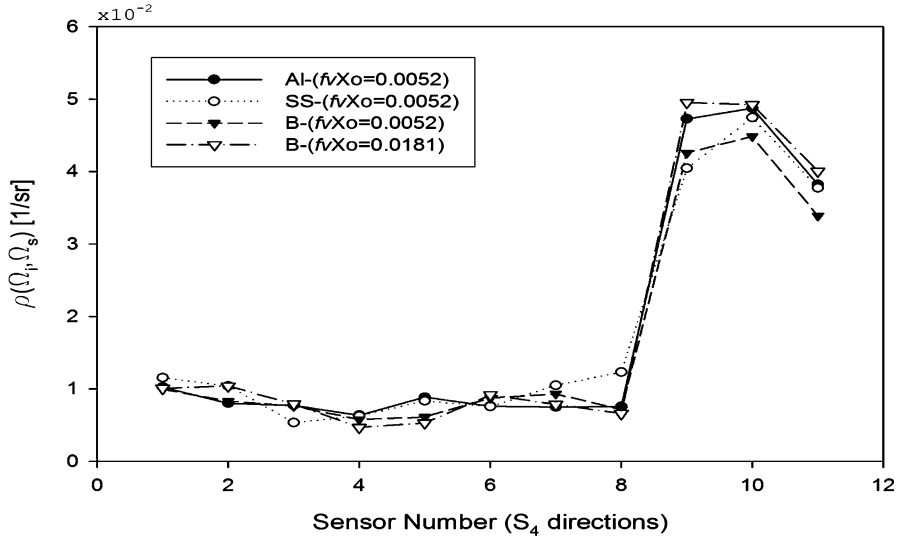

b) Position 1 + 90 deg CW

Fig. 9 Biangular reflectance as a function of the detector number of Durablanket S insulation using various backing (secondary) surfaces with incident angle of Θ = 25 deg and Φ = 315 deg (Port 12).

the absorption coefficient $\kappa_{a\lambda}$, where the sum of the two yields the spectral extinction coefficient β_λ.

The reflectance function (BRDF) governs nonideal radiative reflective properties. The boundary condition for intensity when the reflector is an opaque surface with arbitrary properties[2] can be written as

$$I_\lambda(r,\Omega) = \varepsilon_\lambda I_b(r) + \int_{\Omega'<0} |n\cdot\Omega'|\rho''_\lambda(r,\Omega',\Omega) I_\lambda(r,\Omega')\,\mathrm{d}\Omega' \quad (12)$$

where $I_\lambda(r,\Omega)$ is the intensity leaving a surface at a certain boundary location, $\rho(r,\Omega'\Omega)$ is the biangular reflectance distribution function, n is the unit normal vector at the boundary location, and ε_λ is the emissivity of the surface.

Following Fiveland,[34] Eq. (11) in Cartesian coordinates can be written for monochromatic or for gray radiation as

$$\xi\frac{\partial I}{\partial x}+\eta\frac{\partial I}{\partial y}+\mu\frac{\partial I}{\partial z} = -\beta I+\frac{\sigma_s}{4\pi}\int_{4\pi} P(\Omega\to\Omega')I\,\mathrm{d}\Omega+\kappa I_b \quad (13)$$

where the phase function is approximated to a linear anisotropic phase function as shown in Eq. (5). The S_N approximation of Eq. (13) in the mth direction can expressed as

$$\xi_m\frac{\partial I^m}{\partial x}+\eta_m\frac{\partial I^m}{\partial y}+\mu_m\frac{\partial I^m}{\partial z} = -\beta I^m + S^m \quad (14)$$

where the source function term S_m, representing radiation entering a beam in the mth direction, in Eq. (14) is approximated by

$$S^m = \kappa I_b + \frac{\sigma_s}{4\pi}\sum_{m'}\varpi_{m'}(1+a_1(\xi_m\xi_{m'}+\eta_m\eta_{m'}+\nu_m\nu_{m'})I^{m'} \quad (15)$$

For a discrete direction Ω_m the values of ξ_m, η_m, and μ_m define the direction cosines of Ω obeying the condition $\xi_m^2+\eta_m^2+\mu_m^2=1$. The prime in Eq. (15) denotes the direction of incoming radiation contributing to the m direction.

The discrete boundary conditions can be formulated such, that is, for a nonemitting reflecting west boundary:

$$I^m(r,\Omega) = \sum_{\substack{m'\\ \eta_{m'}<0}}\varpi_m\eta_{m'}\rho''(r,m',m)I^{m'} \quad (16)$$

The second term of the right-hand side in Eq. (16) represents the reflected radiation flux extended over the 2π incoming directions.

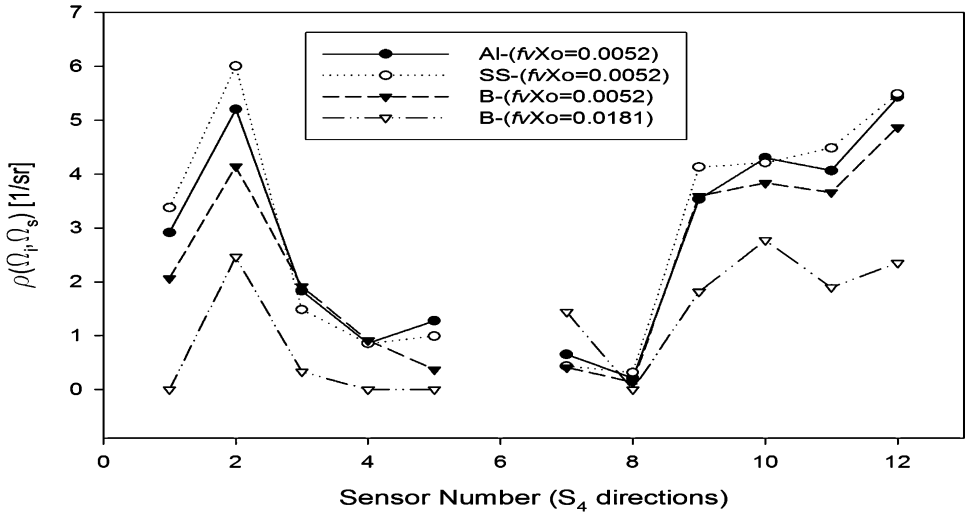

a) Position 1

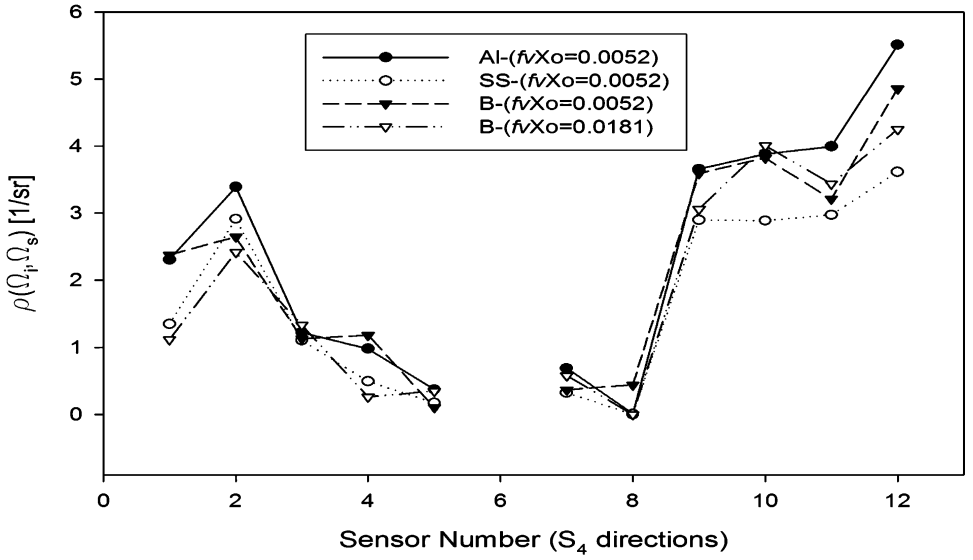

b) Position 1 + 90 deg CW

Fig. 10 Biangular reflectance as a function of the detector number of Durablanket S insulation using various backing (secondary) surfaces with incident angle of Θ = 73 deg and Φ = 162 deg (Port 6).

For a specular and diffuse reflecting surface on the west wall boundary, Eq. (16) is transformed as

$$I^m(r,\Omega) = \varepsilon I_b + \frac{\rho^d}{\pi} \sum_{\substack{m' \\ \eta_{m'}<0}} \varpi_{m'} \eta_{m'} I_{m'} + \rho^s I_{m'} \qquad (17)$$

with $I_{m'}$ as the intensity leaving in the specular direction. Note that, in general, it is not possible to numerically extract the specular term from the bidirectional term under the integral in Eq. (16); therefore, the specular angle must be manually removed even if the reflectance remains under the integral.

Discretization of Equations

Integrating Eq. (14) over the control volume depicted in Fig. 11, a discretized equation is generated as

$$\xi_m A_x \left(I_f^m - I_b^m\right) + \eta_m B_y \left(I_e^m - I_w^m\right) + \mu_m C_z \left(I_n^m - I_s^m\right)$$
$$= -\beta V_p I_p^m + \kappa V_p I_{\text{bp}} + V_p \frac{\sigma_s}{4\pi} \sum_{m'} \varpi_{m'} P(m',m) I_p^{m'} \qquad (18)$$

where V_P is the volume of the control at the point of analysis.

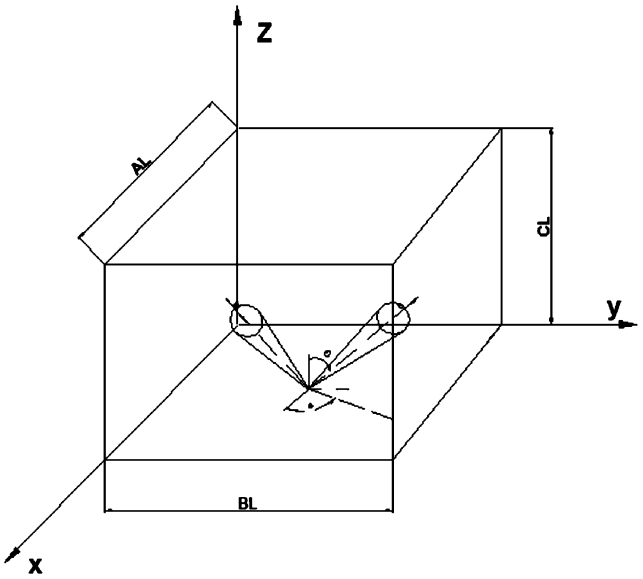

Fig. 11 Rectangular coordinate system.

Each of the control volume intensities can be related to one another by interpolation as the following equation[34]:

$$I_p^m = \Psi I_f^m + (1-\Psi) I_b^m = \Psi I_n^m + (1-\Psi) I_s^m = \Psi I_e^m + (1-\Psi) I_w^m \tag{19}$$

The preceding equations are used to solve for the unknown intensities at the forward, north, and east sides of each one of the control volumes that compose the medium. Thus,

$$I_p^m = \frac{\xi_m A_x I_b^m + \eta_m B_y I_w^m + \mu_m C_z I_s^m + \Psi S_m V_p}{\xi_m A_x + \eta_m B_y + \mu_m C_z + \Psi \beta V_p} \tag{20}$$

where the quantity S_m is defined by Eq. (15).

Positive direction cosines are to be used in Eq. (19). The scalar ψ represents a differencing scheme. For $\psi = \frac{1}{2}$ Larthrop's[30] second-order differencing scheme is obtained. Different schemes are obtained for $\frac{1}{2} < \psi < 1$.

Solution

To completely avoid singularities, which can occur using some direction schemes, the radiation intensity in Eq. (11) is split into eight octants[35]; this is equivalent to applying the absolute values in Eq .(20). Preserving intensity by octant also allows easier numerical testing of symmetries and specular effects. Intensities for each of the octants, A^m through H^m, are denoted for each octal intensity, such as A^m represents the natural (x, y, z) octant arising from positive direction cosines and B^m as $(x, y, -z)$ and so on.

Therefore, eight sets of intensity equations based on Eqs. (20) are created (see Fig. 12). For instance, the intensity equation for octant 1 would be

$$A_p^m = \frac{\xi_m A_x A_b^m + \eta_m B_y A_b^m + \mu_m C_z W_s^m + \Psi S_m V_p}{\xi_m A_x + \eta_m B_y + \mu_m C_z + \Psi \beta V_p} \tag{21}$$

with

$$A_p^m = \Psi A_f^m + (1-\Psi) A_b^m = \Psi A_n^m + (1-\Psi) A_s^m = \Psi A_e^m + (1-\Psi) A_w^m \tag{22}$$

and

$$I(x, y, z, \theta, \Phi) = A(x, y, z, \theta, \Phi) \qquad 0 < \theta < \pi/2, \qquad 0 < \Phi < \pi/2$$

where the reference faces for octant 1 are the backward, south, and west sides of the cubical geometry. For the other octal intensities the equations would look similar to Eqs. (21) and (22), but the reference faces are the faces adjacent to the axis of the coordinate systems. Using the new set of octal intensities, Eq. (15) can be expanded to obtain

$$S_{ip}^m = \kappa I_b + \frac{\sigma_s}{4\pi} \left\{ \sum_{m'} \varpi_{m'} \left[1 + a_1 (\xi_m \xi_{m'} + \eta_m \eta_{m'} + \nu_m \nu_{m'})_x \times \left(A_p^{m'} + B_p^{m'} + C_p^{m'} + D_p^{m'} + E_p^{m'} + F_p^{m'} + G_p^{m'} + H_p^{m'} \right) \right] \right\} \tag{23}$$

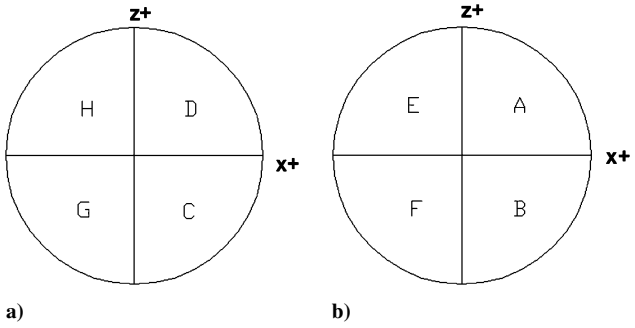

Fig. 12 Octal intensities at the west boundary side for the source function development: a) incident and b) leaving.

where i represents the octal intensity (from A^m to H^m) in this discussion. Equation (23) must be set for each one of the eight octal intensities in order to account for the angular variation in linear anisotropic phase function.

S_4 Approximation

In the preceding paragraphs a quadrature scheme was chosen for its unique qualities to integrate the source function for a good variety of phase functions, including simple scattering functions as the linear anisotropic scattering phase function. This quadrature scheme establishes three directions per octant to make a total of 12 for a hemisphere from which the boundary analysis is made.

To explain the preceding concept further, the boundary condition at the west side (Fig. 12) is expanded. The octal incident and leaving intensities at the west boundary are the intensities pointing at the negative and positive y direction, respectively. Thus, for leaving intensity A^m, Eq. (16) is transformed into

$$A_p^m(r, \Omega) = \sum_{\substack{m' \\ \eta_{m'} < 0}} \varpi_{m'} \eta_{m'} \rho''(r_p, m', m) \left(C_p^{m'} + D_p^{m'} + G_p^{m'} + H_p^{m'} \right) \tag{24}$$

where r_p symbolizes that the reflectivity depends also of the octal intensity. Separating the second term of right-hand side of Eq. (24) into its components, then for the S_4 approximation one obtains

$$\sum_{\substack{m' \\ \eta_{m'} < 0}} \varpi_{m'} \eta_{m'} \left[\rho_C(m', m) C_p^{m'} + \rho_D(m', m) D_p^{m'} + \rho_G(m', m) G_p^{m'} + \rho_H(m', m) H_p^{m'} \right] \tag{25}$$

Expanding for all leaving and incident directions, one obtains a directional reflectance function that considers the reflection from all incident and leaving intensities. Thus, the reflectance function for a particular octal intensity can be represented as a uniform matrix

$$\rho_{i,l}(\Omega_{m'}, \Omega_m) = \begin{bmatrix} \rho_{i,l}(1,1) & \rho_{i,l}(1,2) & \rho_{i,l}(1,3) \\ \rho_{i,l}(2,1) & \rho_{i,l}(2,2) & \rho_{i,l}(2,3) \\ \rho_{i,l}(3,1) & \rho_{i,l}(3,2) & \rho_{i,l}(3,3) \end{bmatrix} \tag{26}$$

with i representing the boundary side of incidence and l representing the intensity incident upon the wall i. There are 144 possible reflectance combinations in a boundary, including 12 of retroreflection. These reflectance directions are expressed in $16, 3 \times 3$ matrices, which will complete the 144-reflectance combinations.

For the specularly reflecting, diffusively emitting opaque boundary conditions model, the boundary is discretized by taking into account the incoming direction intensity for the respective octant that will produce a specular reflection at the octal concerning the boundary and summing all contributions for diffuse reflection. At the west boundary wall intensity A^m is formulated as

$$A_w^m = \varepsilon I_b + \rho^s H_p^m + \frac{\rho^d}{\pi} \sum_{\substack{m' \\ \eta_{m'} < 0}} \varpi_{m'} \eta_{m'} \left(C_p^{m'} + D_p^{m'} + G_p^{m'} + H_p^{m'} \right) \tag{27}$$

Intensity H_p^m is the intensity that will produce a specular reflection leaving in direction of A_w^m. This intensity was selected by taking into account the spherical geometry of radiation intensities (all octal intensities forming a sphere) and the plane of incidence of the specular ray leaving in the desired direction of intensity A^m.

Because the solution in DOM is through continuous iteration, the calculations must be performed by step-by-step process based on previous developments. Comparisons for the source term and

incident radiation for current and previous iterations are made until convergence agreement of less than 0.01%.

Once the intensity distribution along the center nodes is determined, quantities of engineering interest (i.e., heat flux, incident intensity, source term distributions) are readily computed.

Treatment of Collimated Irradiation to Determine the Reflectance Function

There exist many situations when a collimated monodirectional flux is incident to a scattering boundary layer such as surface coatings, a planetary atmosphere, insulation shielding, etc., for which the radiation transfer is not azimuthally symmetric. For the current work the experiment consists of this condition (whereas the motivating fire barrier problem does not).

Consider the problem of a collimated incident intensity flux of magnitude q_0 incident on a medium with suspended particles (or fibers) having a relative refractive index of unity with respect to the surrounding boundaries.

The direction of incidence is given by the coordinate system (ξ_0, η_0, μ_0). Treating the collimated irradiation flux as a source term in the transfer equation, then $q_0 \exp[\int \beta \, \mathrm{d}(C_L - z)]$ is the attenuated flux at any specific depth. The contribution to the scattered radiation field in the direction (ξ_0, η_0, μ_0) is[36]

$$Sc = \frac{\sigma_s}{4\pi} P(\Omega' \to \Omega) q_0 \exp\left[\int \beta \, \mathrm{d}(C_L - z)\right] \tag{28}$$

and the RTE becomes

$$(\Omega \cdot \nabla) I_\lambda(r, \Omega) = -(\kappa_\lambda + \sigma_{s\lambda}) I_\lambda(r, \Omega) + \kappa_\lambda I_b(r) + \frac{\sigma_{s\lambda}}{4\pi} \int_{\Omega' \to 4\pi} I_\lambda(r, \Omega) P(\Omega' \to \Omega) \, \mathrm{d}\Omega' + Sc \tag{29}$$

Discretizing the preceding equation leads to the same octal equations as shown before except that the source function will have the collimated term to be evaluated. Because the intensity was spilt into eight octants, the collimated incident flux of magnitude q_0 must also be divided into the same number of octants. Thus, Eq. (23) is transformed into

$$S^m_{\mathrm{ip}} = \kappa I_b + \frac{\sigma_s}{4\pi} \left\{ \sum_{m'} \varpi_{m'} \left[1 + a_1 (\xi_m \xi_{m'} + \eta_m \eta_{m'} + \mu_m \mu_{m'})_x \times \left(A_p^{m'} + B_p^{m'} + C_p^{m'} + D_p^{m'} + E_p^{m'} + F_p^{m'} + G_p^{m'} + H_p^{m'} \right) \right] \right\} + \frac{\sigma_s}{4\pi} \left(\frac{q_0}{8} \right) \exp\left[\int \beta \, \mathrm{d}(C_L - z) \right] \times [1 + a_1 (\xi_m \xi_0 + \eta_m \eta_0 = \mu_m \mu_0)] \tag{30}$$

The last term in Eq. (30) is the source function caused by the collimated irradiation flux, where i represent the octal intensity (from A^m to H^m) in discussion. Equation (30) must be set for each one of the eight octal intensities in order to account for the angular variation in linear anisotropic phase function.

For some situations in which the emission term is nonexistent and the monodirectional collimated incident flux is the only source of radiation, the scattered intensities leaving the top and low boundaries are the unknowns to the problem. These unknowns are represented by the reflectance function for the respective boundary. Thus, for this problem

$$\rho(\theta_0, \phi_0; \theta_0, \phi_0) = \frac{\pi I[C_L, (\theta_s, \phi_s > 0)]}{\Delta\Omega q_0} \tag{31}$$

The intensity I in Eq. (31) represents the octal intensities A, D, E, and H.

To validate the accuracy of the three-dimensional formulation with collimated irradiation at the top boundary, the diffuse reflectivity and diffuse transmissivity were calculated for a purely scattering slab ($\omega = 1$) subject to normal incident flux ($\xi_o = 0$, $\eta_o = 0$, $\mu_o = -1$) for different types of scattering situations. These results (Fig. 13) were compared with Ref. 36 (except the anisotropic backward scattering) and to a one-dimensional formulation using the S_8 quadrature. The result for the three-dimensional formulation with dominant z direction agrees very well with the other two comparison parameters. The diffuse transmissivity for the forward scattering is off by 2% because of geometrical effects and because some intensity

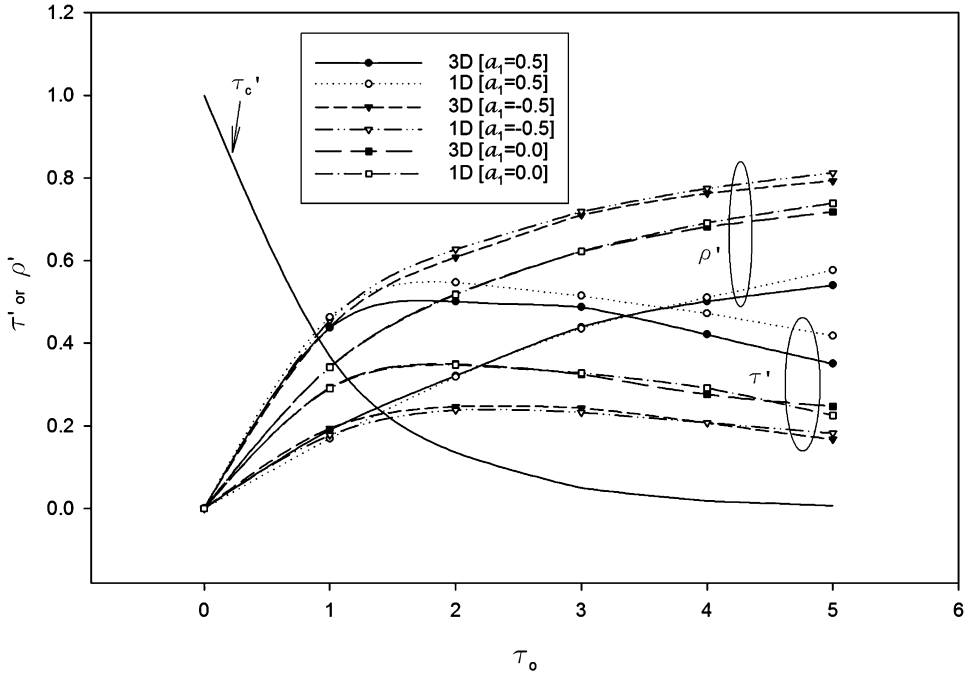

Fig. 13 Comparison of reflectivity and transmissivity for a slab subject to collimated incident irradiation with Brewster[36] for conservative isotropic ($a_1 = 0$), anisotropic forward scattering ($a_1 = 0.5$), and anisotropic backward scattering ($a_1 = -0.5$), using S_N method ($N = 8$) for a one- and three-dimensional formulation (dominant z direction): ($\omega = 1$, $\xi_o = 0$, $\eta_o = 0$, $\mu_o = -1$).

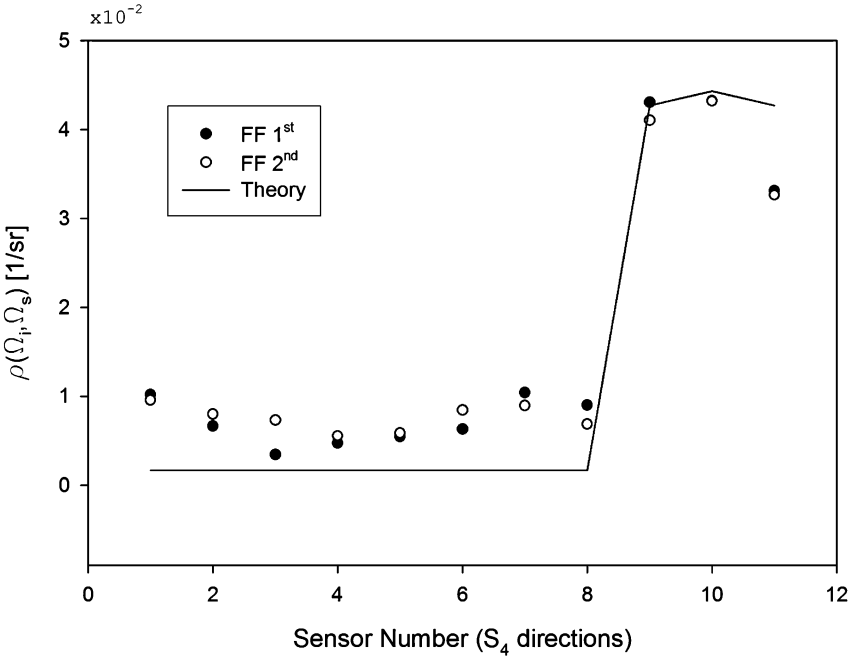

Fig. 14 Biangular reflectance as a function of the detector number of Durablanket S insulation with incident angle of Θ = 25 deg, Φ = 315 deg (Port 12), and $f_v X_0 = 0.0052$.

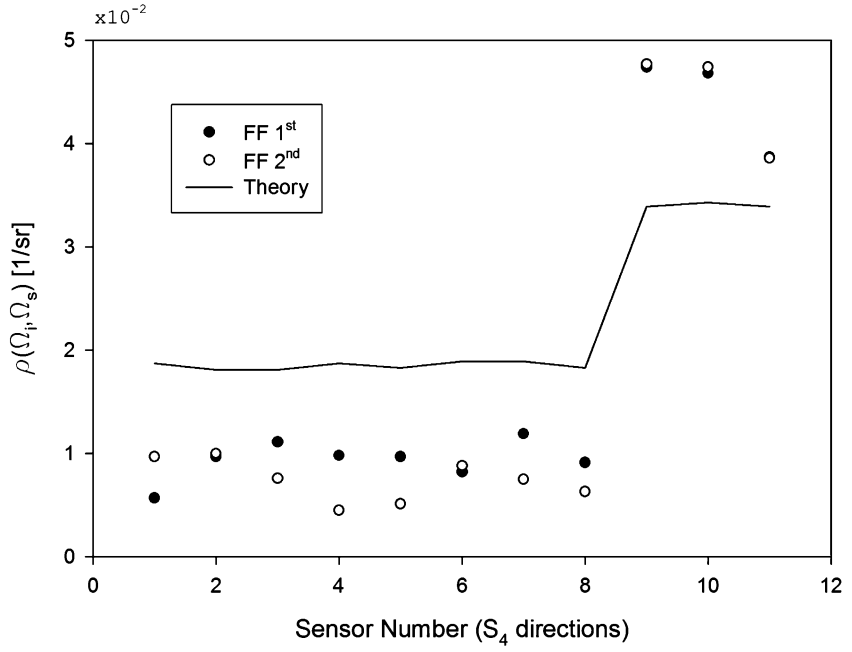

Fig. 15 Biangular reflectance as a function of the detector number of Durablanket S insulation with incident angle of Θ = 25 deg, Φ = 315 deg (Port 12), and $f_v X_0 = 0.0181$.

rays are leaving to the other four boundaries. The one-dimensional results overlap the results from Ref. 36. τ_c' is defined as the collimated irradiation transmissivity, defined as $\exp[-\beta(C_L/\mu_0)]$.

Reflectance Results and Discussion

Biangular reflectance data for a specimen of Durablanket S with a thickness of $f_v X_0 = 0.0052$ are shown in Fig. 14. The solid curve is from the data calculated using the preceding theoretical model for the same value of the fiber volume fraction-thickness product $f_v X_0$ as it was measured for the test specimen. The calculation was performed setting the semitransparent boundaries at the top and bottom of the three-dimensional media using the gray values for the insulation. The magnitude of the irradiation flux was specified together with the beam width and the cosine vector values that specify the beam direction. A specular fraction value is given to the incoming irradiation beam. Setting up a value less than one will provide with a portion of the ray to reflect specularly at the impinged wall while the rest is transmitted to the media and reflected diffusively.

Experimental data (using the Reflect IR-P1S) lie above the calculated values in the diffuse part (directions 1–8), although a better match is obtained at the specular directions (directions 9–11). Although the orientation effect is small for the test materials, the same figure also shows that the linear anisotropic model does not account for the effects of specimen orientation.

Experimental data illustrating the reflectance function for a different fiber volume fraction-thickness product $f_v X_0$ are presented in Fig. 15. The results show that the calculated reflectance follows the trend obtained in the experimental trials but with larger

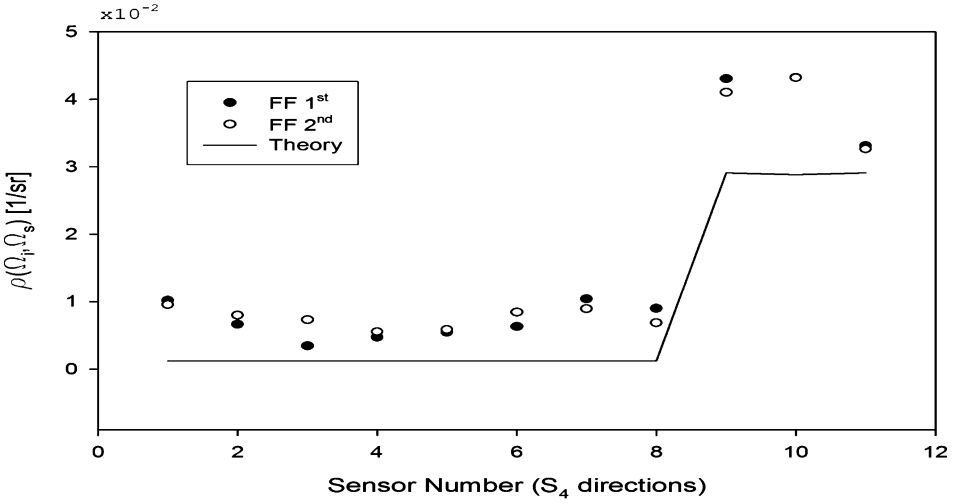

a) Black surface backing

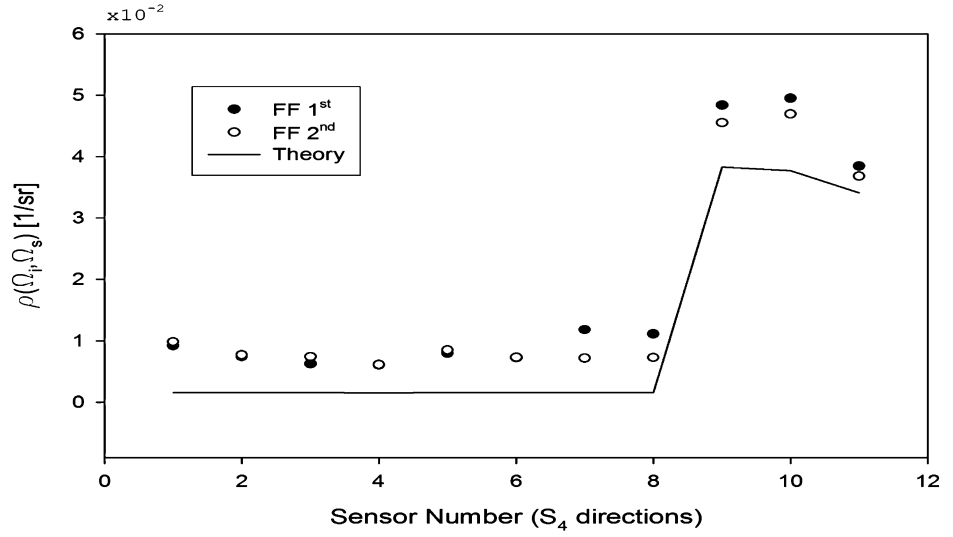

b) Aluminum-foil surface backing

Fig. 16 Biangular reflectance as a function of the detector number of Durablanket S insulation with incident angle of $\Theta = 25$ deg, $\Phi = 315$ deg (Port 12), and $f_v X_0 = 0.0052$.

diffuse values and lower specular values. The calculated result shows that the discrete ordinate method tries to distribute the scattered energy evenly around the hemisphere particularly when large optical thicknesses are provided. The specular fraction value for the calculated data was lower than the one used in data depicted in Fig. 14.

Comparisons of theoretical model predictions using the 144 different reflectance directions at the bottom boundary with the experimental data for the biangular reflectance for two different values of $f_v X_0$ are shown in Fig. 16. The agreement between the experiment (using the Reflect IR-P1S) and theory for the case of using the black backing surface reflectance is shown in Fig. 16a. Figure 16b depicts the agreement between the experimental data and the calculated data using the reflectance directions of the aluminum foil as backing at the bottom boundary for the same fiber volume fraction-thickness product $f_v X_0$ as Fig. 16a. Figure 17 shows reflectance function trend for a higher optical thickness sample.

Poor agreement between the experimental data and the theory is found for the biangular reflectance data when the incoming radiation is at the lower angles of the quadrature as shown in Fig. 18. Figure 18a shows that a similar trend is followed by the calculated results in comparison to the experimental data while using the reflectance directions for the aluminum surface at the bottom boundary, and Fig. 18b shows the results when using a black-anodized surface at the bottom. One of the reasons of the poor agreement could be that the method tends to redistribute the energy evenly around the hemisphere as stated before. Additionally, the simple form of the phase function does not usually capture the two-dimensional scattering behavior of fibers, which at near grazing angles becomes important.

In spite of the use of a simpler anisotropic function, a good qualitative agreement for the prediction of reflectance function values in randomly oriented fibrous materials throughout the hemisphere when for near normal incident angles has been demonstrated. However, at bigger incident angles fiber surface effects and the difference between the scattering directions around the hemisphere (forward and backward) relative to the slab geometry and those in relation with a single fiber are of great consideration, which could translate into disparities in the scattering phenomena. Also, the scattering mechanisms of the fiber with respect to the boundary are related to the radiation scattered into the opposite hemisphere from that containing the incident direction, which results in uncertainties of the reflectance data. The scattering phenomena cannot be provided just by a single number (scattering coefficient), and the use of the exact phase function would probably enhance the agreement between the experimental and the theoretical data. However, the use of the biangular reflectance function data as boundary condition helps to diminish, in some degree, the uncertainty of the model.

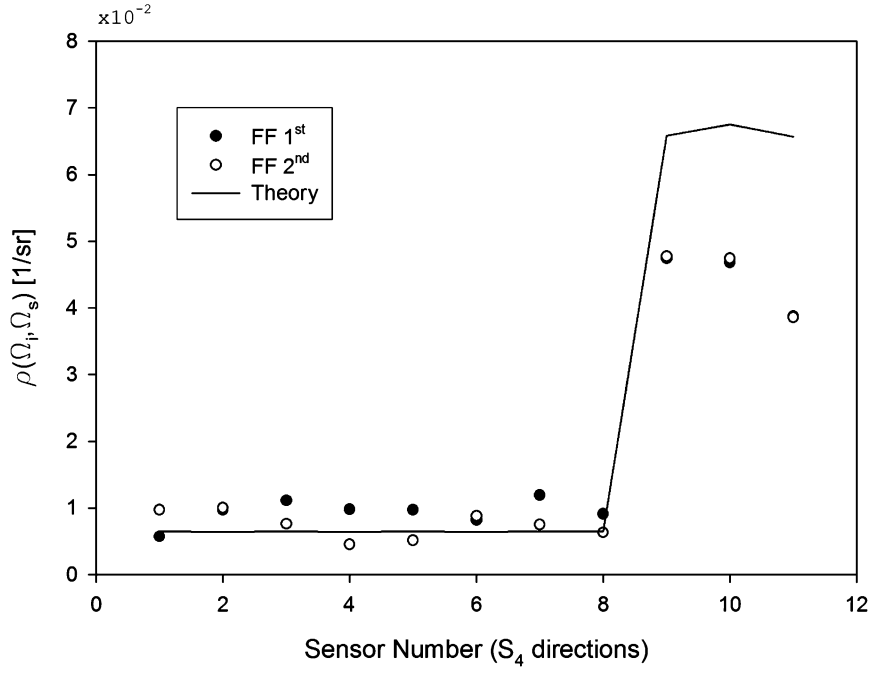

Fig. 17 Biangular reflectance as a function of the detector number of Durablanket S insulation with incident angle of Θ = 25 deg, Φ = 315 deg (Port 12), and $f_\nu X_0 = 0.0181$.

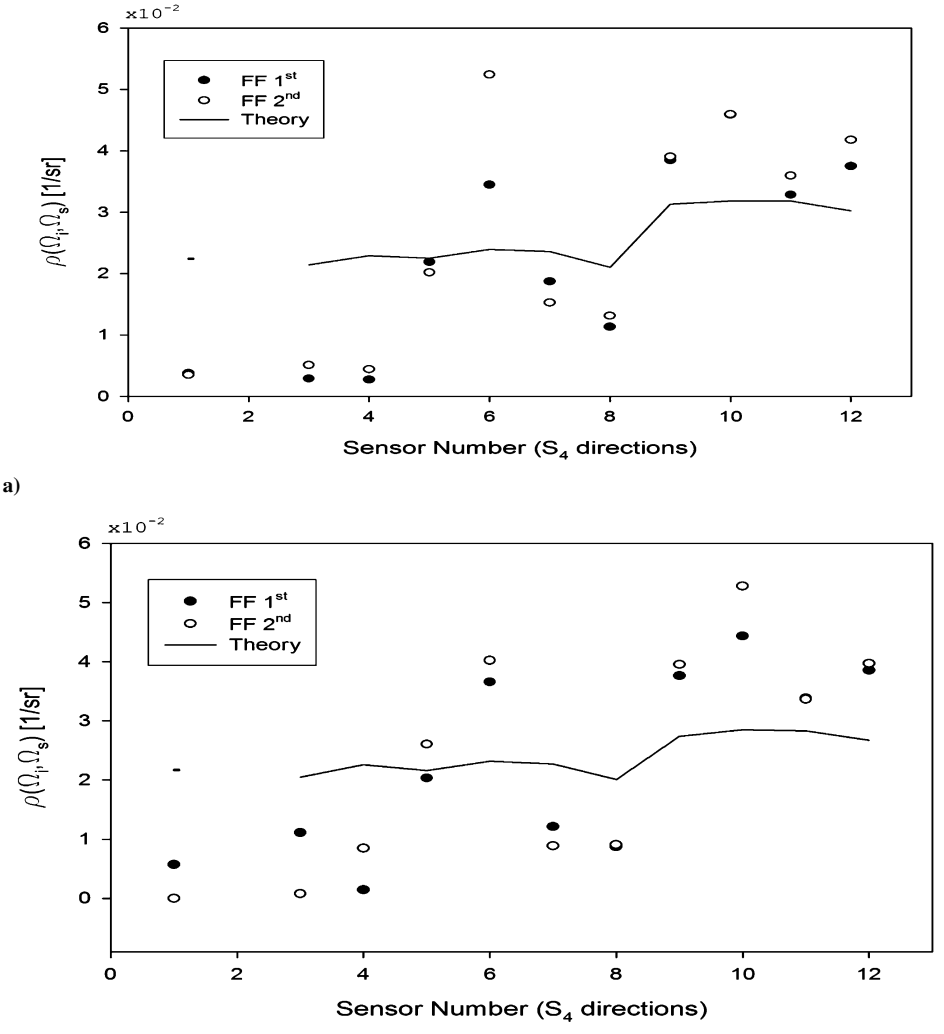

Fig. 18 Biangular reflectance as a function of the detector number of Durablanket S insulation with incident angle of Θ = 73 deg, Φ = 342 deg (Port 2), and $f_\nu X_0 = 0.0052$: a) aluminum-foil surface backing and b) black-anodized surface backing.

V. Conclusions

The DOM-hemispherical scatterometer prototype has proved itself as a device to measure the reflectance function but also to investigate the surface defects and scattering effects in the infrared region. The versatility of choosing a discrete ordinates quadrature can make the apparatus as an experimental tool to be included in heat-transfer calculations using the discrete ordinate method. These results also provide a simplified measure of scattering data for surface and pattern recognition ("on-the-fly" measurement) and can be used as a reference tool for machining and surface finish process using grayscale data.

The apparatus can easily be adapted by more powerful types of sensors and light sources, which in turn will make it as a important tool for studies purposes. Furthermore, increasing the quadrature scheme to a one of higher order will uncover more surface effects, that is, off specular shifting, and will be an excellent parameter for theoretical comparisons.

Finally, the changes with respect to the spectral bands are not strong and barely noticeable. As just stated, the results and claims will be greatly enhanced with the use of well-defined spectral sources.

This biangular reflectance model has demonstrated its potential to resolve Cartesian radiation heat-transfer problems in more depth than other particular models. It has shown the capabilities to set up most common boundary conditions including the biangular reflectance model in a straightforward manner. It can also be easily adapted to more complicated phase functions.

The good agreement among the theoretical data demonstrates the validity of the theoretical formalisms expressed by Fiveland[34] and Sutton and Kamath[35] for their respective radiation heat-transfer situations. It has also shown good promise with respect to the easily development of biangular reflectance boundary conditions for the S_4 approximation.

For this type of calculation, the S_4 DOM method has shown to distribute the energy around the hemisphere. This happens because of the single weighting value to describe the hemisphere of radiation and to the inherent directional biasing of the quadrature scheme. A different or higher scheme could help to overcome this situation at the expense of grater computational effort.

Acknowledgments

We thank all of the people who collaborated in some technical details during the research leading to this work. Especially we thank T. J. Love Jr. and Siu-Chun Lee at the Applied Sciences Laboratory, Industry, California, for their invaluable suggestions.

References

[1]Love, T. J., *Radiative Heat Transfer*, Merrill, Columbus, OH, 1968, pp. 38–45.

[2]Modest, M. F., *Radiative Heat Transfer*, McGraw–Hill, New York, 1993, pp. 84–89, 542–547.

[3]Tang, K., Dimenna, R. A., and Buckius, R. O., "Regions of Validity of the Geometric Optics Approximation for Angular Scattering from Very Rough Surfaces," *International Journal of Heat and Mass Transfer*, Vol. 40, No. 1, 1997, pp. 49–59.

[4]Davies, H., "The Reflection of Electromagnetic Waves From a Rough Surface," *Proceedings of the Institution of Electrical Engineers*, Vol. 101, No. 4, 1954, pp. 209–214.

[5]Bennet, H. E., and Porteous, J. O., "Relation Between Surface Roughness and Specular Reflectance at Normal Incidence," *Journal of the Optical Society of America*, Vol. 51, No. 2, 1961, pp. 123–129.

[6]Beckmann, P., and Spizzinno, A., *The Scattering of Electromagnetic Waves from Rough Surfaces*, Pergamon, New York, 1963, pp. 110–124.

[7]Torrance, K. E., and Sparrow, E. M., "Theory for Off-Specular Reflection from Roughened Surfaces," *Journal of the Optical Society of America*, Vol. 9, No. 9, 1967, pp. 110–124, 1105–1111.

[8]Smith, A. M., Muller, P. R., Frost, W., and Hsia, H. M., "Super- and SubSpecular Maxima in the Angular Distribution of Polarized Radiation Reflected from Roughened Dielectric Surfaces," *Heat Transfer and Spacecraft Thermal Control*, edited by J. W. Lucas, MIT Press, Pasadena, CA, 1971, pp. 249–269.

[9]Tang, K., Kawka, P. A., and Buckius, R. O., "Geometric Optics Applied to Rough surfaces Coated with an Absorbing Thin Film," *Journal of Thermophysics and Heat Transfer*, Vol. 13, No. 2, 1999, pp. 169–175.

[10]Tang, K., Yang, Y., and Buckius, R. O., "Theory and Experiments on Scattering from Rough Surfaces," *Annual Review of Heat Transfer*, Vol. 10, Begell House, New York, 1999, pp. 101–140.

[11]Germer, T. A., "Polarized Light Scattering by Microroughness and Small Defects in Dielectric Layers," *Journal of the Optical Society of America*, Vol. 18, No. 6, 2001, pp. 1279–1288.

[12]Larkin, B. K., and Churchill, S. W., "Heat Transfer by Radiation Through Porous Insulations," *American Institute of Chemical Engineering Journal*, Vol. 5, No. 5, 1965, pp. 467–474.

[13]Tong, T. W., "Thermal Radiation in Fibrous Insulations," Ph.D. Dissertation, Dept. of Mechanical Engineering, Univ. of California, Berkeley, CA, June 1980.

[14]Tong, T. W., and Tien, C. L., "Radiative Heat Transfer in Fibrous Insulations—Part I: Analytical Study," *Journal of Heat Transfer*, Vol. 105, Feb. 1983, pp. 70–85.

[15]Lee, S. C., "Radiative Transfer Through a Fibrous Medium: Allowance for Fiber Orientation," *Journal of Quantitative Spectroscopy and Radiative Transfer*, Vol. 36, No. 3, 1986, pp. 253–263.

[16]Lee, S. C., "Scattering Phase Function for Fibrous Media," *International Journal of Heat and Mass Transfer*, Vol. 33, No. 10, 1990, pp. 2183–2190.

[17]Lee, S. C., "Scattering by Closely-Spaced Radially-Stratified Parallel Cylinders," *Journal of Quantitative Spectroscopy and Radiative Transfer*, Vol. 48, No. 2, 1992, pp. 119–130.

[18]Lee, S. C., and Cunnington, G. R., "Conduction and Radiation Heat Transfer in High Porosity Fiber Thermal Insulation," *Journal of Thermophysics and Heat Transfer*, Vol. 14, No. 2, 2000, pp. 121–136.

[19]Roux, J. A., and Smith, A. M., "Biangular Reflectance for an Absorbing and Isotropically Scattering Medium," *AIAA Journal*, Vol. 23, No. 4, 1985, pp. 624–628.

[20]Rokhsaz, F., and Dougherty, R. L., "Radiative Heat Transfer Within a Finite Plane-Parallel Medium Exhibiting Fresnel Reflection at a Boundary," *Heat Transfer Phenomena in Radiation, Combustion, and Fires*, edited by R. K. Shah, HTD-Vol. 106, American Society of Mechanical Engineers, Fairfield, NJ, 1989.

[21]Wu, C.-Y., and Liou, B.-T., "Discrete-Ordinate Solutions for Radiative Transfer in a Cylindrical Enclosure with Fresnel Boundaries," *International Journal of Heat and Mass Transfer*, Vol. 40, No. 10, 1997, pp. 2467–2475.

[22]Germer, T. A., "Multidetector Hemispherical Polarized Light Scattering Instrument," *Rough Surface Scattering and Contamination*, edited by P.-T. Chen, Z.-H. Gu, and A. A. Maradudin, SPIE Optical Engineering Press, Bellingham, WA, Vol. 3784, 1999, pp. 296–303.

[23]Sánchez, M. A., "A Study of Directional Radiative Properties of Thermal Fire Barriers," Ph.D. Dissertation, School of Aerospace and Mechanical Engineering, Univ. of Oklahoma, Norman, OK, Dec. 2002.

[24]Kerker, M. C., *The Scattering of Light and Other Electromagnetic Radiation*, Academic Press, New York, 1969, Chap. 6.

[25]Choy, T. C., *Effective Medium Theory. Principles and Applications*, Clarendon, Oxford, England, U.K., 1999, pp. 20–45.

[26]Palik, E. D., *Handbook of Optical Constants of Solids II*, Academic Press, New York, 1991, p. 761.

[27]Swathi, P. S., and Tong, T. W., "A New Algorithm for Computing the Scattering Coefficients of Highly Absorbing Cylinders," *Journal of Quantitative Spectroscopy and Radiative Transfer*, Vol. 40, No. 4, 1988, pp. 525–530.

[28]Caplinger, G. D., Sutton, W. H., Spindler, R., and Golke, H., "Transient Heat Transfer for Layered Ceramic Insulation and Stainless Steel Foil Fire Barriers," *Journal of Heat Transfer*, Vol. 121, Aug. 1999, pp. 1059–1066.

[29]Fiveland, W. A., "The Selection of Discrete Ordinate Quadrature Sets for Anisotropic Scattering," *Fundamentals of Radiation Heat Transfer*, Vol. HTD-160, American Society of Mechanical Engineers, Fairfield, NJ, 1991, pp. 89–96.

[30]Larthrop, K. D., and Carlson, B. G., "Discrete Ordinates Angular Quadrature of the Neutron Transport Equation," Los Alamos Scientific Lab., Rept. LA-3186, UC-32, Mathematics and Computers TID-4500 (36th edition), Los Alamos, NM, Sept. 1964.

[31]"Standard Practice for Angle Resolved Optical Scatter Measurements on Specular or Diffuse Surfaces," American Society for Testing and Materials, ASTM Standard E 1392-90, Philadelphia, 1991.

[32]Ford, J. N., Tang, K., and Buckius, R. O., "Fourier Transform Infrared System Measurement of the Bidirectional Reflectivity of Diffuse and Grooved Surfaces," *Journal of Heat Transfer*, Vol. 117, No. 4, 1995, pp. 955–962.

[33]Kim, J. H., Simon, T. W., and Viskanta, R., "Journal of Heat Transfer Policy on Reporting Uncertainties in Experimental Measurements and Results," *Journal of Heat Transfer*, Vol. 115, Feb. 1993, pp. 5, 6.

[34]Fiveland, W. A., "Three-Dimensional Radiative Heat Transfer Solutions by the Discrete Ordinates Method," *Journal of Thermophysics and Heat Transfer*, Vol. 2, No. 4, 1988, pp. 309–316.

[35]Sutton, W. H., and Kamath, R. S., "Participating Radiative Heat Transfer in a Three-Dimensional Rectangular Medium with Layered Properties," American Society of Mechanical Engineers, Paper 86-HT-25, Fairfield, NJ, June 1986.

[36]Brewster, M. Q., *Thermal Radiative Transfer and Properties*, Wiley-Interscience, New York, 1992, pp. 125–130.